

# Dielectric Profile of Interfacial Water and its Effect on Double Layer Capacitance

Douwe Jan Bonthuis<sup>1</sup>, Stephan Gekle<sup>1</sup> & Roland R. Netz<sup>2</sup>

<sup>1</sup>Physik Department, Technische Universität München, 85748 Garching, Germany

<sup>2</sup>Fachbereich Physik, Freie Universität Berlin, 14195 Berlin, Germany

---

► **Abstract.** The framework for deriving interfacial dielectric profiles from bound charge distributions is established and applied to molecular dynamics simulations of water at hydrophobic and hydrophilic surfaces. In conjunction with a modified Poisson-Boltzmann equation, the trend of experimental double layer capacitances is well reproduced. We show that the apparent Stern layer can be understood in terms of the continuous dielectric profile of pure water.

---

One of the most salient properties of water is its high molecular polarity. As a result, electrostatic interactions in aqueous environments are drastically modified with profound implications for the behavior of ions, proteins and membranes in solution [1]. Experiments and simulations have shown that the dielectric function of homogeneous water exhibits two singularities for wave vectors at molecular length scales, indicating anomalous screening effects in bulk [2]. To what extent interfacial water exhibits similar anomalies is less clear [3]. Experimental capacitance studies have led Stern to propose a model for an aqueous interface where the dielectric constant is reduced over a nanoscopic width [4]. Whether this layer reflects ionic or rather intrinsic water properties is not specified in the original Stern model. However, recent terahertz spectroscopy experiments have shown that the dielectric properties of water itself are modified at interfaces within a layer of molecular size [5]. Without calculating the dielectric profile, it was shown how the Stern layer contribution to the capacitance emerges from a non-local dielectric function [6], also for non-linear response [7]. Using approximate statistical mechanical methods, it has been shown that the lowering of the interfacial capacitance for a dipolar fluid is due to molecular ordering and orientation [8]. However, a method for calculating dielectric profiles from the distribution of partial charge on the water molecules, as well as the profiles themselves, have been lacking so far.

Detailed knowledge of the interfacial dielectric behavior of water is a prerequisite for correct modeling of ion distributions [9] and double layer interactions [10], as well as electrokinetic effects. Similarly, the interfacial dielectric function is a key ingredient to solvent-implicit approaches towards protein and macromolecular modeling [11]. Control over the interfacial dielectric constant is also crucial for a number of industrial applications, including high power and long duration energy storage de-

vices [12]. Finally, dielectric effects are one contribution to the hydration repulsion between polar surfaces [13, 1]. The dielectric properties of interfacial water have been studied using both simulations and analytic approaches. One shortcoming of previous analytic approaches is that the water bulk behavior including the above-mentioned anomaly is typically not accounted for [14, 15]. At the same time, previous simulations with explicit water and ions could not be analyzed within the existing theoretical framework. One reason for the complexity is the appearance of higher order multipole moments, which are particularly essential at interfaces [16].

The purpose of this Letter is threefold: first, we develop the theoretical framework to extract both parallel and perpendicular interfacial dielectric response functions from the bound charge distribution. Quadrupole and higher order moments, which were neglected previously [17], turn out to be crucial. Second, we extract the dielectric response functions using large-scale molecular dynamics (MD) simulations of water and demonstrate that the perpendicular dielectric function exhibits singularities like the non-local bulk dielectric function, whereas the parallel function is smooth. The remarkable differences between hydrophobic and hydrophilic surfaces can be quantified in terms of a dielectric dividing surface, defined similarly to the Gibbs dividing surface. Third, we use a modified Poisson-Boltzmann equation to show that the experimental double layer capacitance can be largely understood by the dielectric profile of pure water.

► **Dielectric Linear Response.** A local change in displacement field  $\mathbf{D}(\mathbf{r})$  is related to a change in electric field  $\mathbf{E}(\mathbf{r}')$  via the non-local dielectric tensor  $\varepsilon_{nl}(\mathbf{r}, \mathbf{r}')$ ,  $\Delta\mathbf{D}(\mathbf{r}) = \varepsilon_0 \int \varepsilon_{nl}(\mathbf{r}, \mathbf{r}') \cdot \Delta\mathbf{E}(\mathbf{r}') d\mathbf{r}'$ , with  $\varepsilon_0$  the permittivity of vacuum. For a homogeneous electric field,  $\Delta\mathbf{E}(\mathbf{r}) = \Delta\mathbf{E}$ , which holds for the averaged tangential field component at planar interfaces as will be discussed

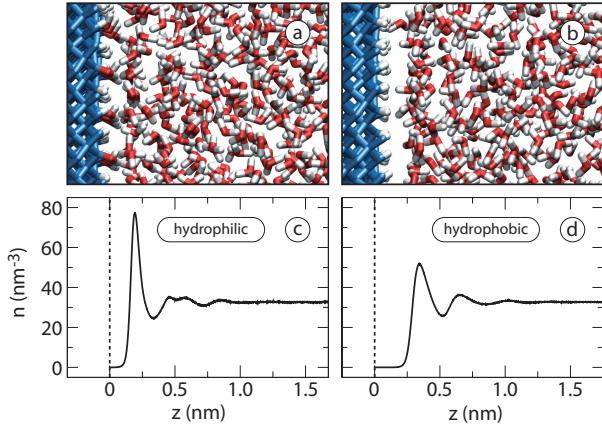


Figure 1: Snapshots from the simulations of the hydrophilic (a) and hydrophobic surface (b) and corresponding water density profiles  $n(z)$  without external electric field (c-d). All graphs have the same  $z$  scale, with  $z = 0$  fixed at the outermost carbon atoms for the hydrophobic and at the oxygen atoms of the hydroxyl groups for the hydrophilic surface.

below, the response function becomes local,

$$\Delta \mathbf{D}(\mathbf{r}) = \varepsilon_0 \varepsilon(\mathbf{r}) \cdot \Delta \mathbf{E}, \quad (1)$$

with  $\varepsilon(\mathbf{r}) = \int \varepsilon_{nl}(\mathbf{r}, \mathbf{r}') d\mathbf{r}'$ . This makes the usual locality assumption  $\varepsilon_{nl}(\mathbf{r}, \mathbf{r}') = \varepsilon(\mathbf{r}) \delta(\mathbf{r} - \mathbf{r}')$  superfluous. The inverse response function  $\varepsilon_{nl}^{-1}(\mathbf{r}, \mathbf{r}')$  is defined by  $\Delta \mathbf{E}(\mathbf{r}) = \varepsilon_0^{-1} \int \varepsilon_{nl}^{-1}(\mathbf{r}, \mathbf{r}') \cdot \Delta \mathbf{D}(\mathbf{r}') d\mathbf{r}'$  [6] and becomes local when  $\mathbf{D}(\mathbf{r})$  is uniform, which holds for the averaged perpendicular component at a planar interface,

$$\Delta \mathbf{E}(\mathbf{r}) = \varepsilon_0^{-1} \varepsilon^{-1}(\mathbf{r}) \cdot \Delta \mathbf{D}, \quad (2)$$

with  $\varepsilon^{-1}(\mathbf{r})$  the inverse dielectric function.

► **Fluctuation-Dissipation Relation.** The electric field is separated into the displacement field  $\mathbf{D}(\mathbf{r})$ , associated with the monopole density, and the polarization  $\mathbf{m}(\mathbf{r})$ , generated by all higher multipole moments,  $\varepsilon_0 \mathbf{E}(\mathbf{r}) = \mathbf{D}(\mathbf{r}) - \mathbf{m}(\mathbf{r})$ . Defining the total polarization in a volume  $\mathcal{V}$  by  $\mathbf{M} = \int_{\mathcal{V}} \mathbf{m}(\mathbf{r}) d\mathbf{r}$ , the change in polarization upon application of an external homogeneous electric field  $\mathbf{F}$ , defined as  $\Delta \mathbf{m}(\mathbf{r}) = \langle \mathbf{m}(\mathbf{r}) \rangle_{\mathbf{F}} - \langle \mathbf{m}(\mathbf{r}) \rangle_0$ , is given by [17, 18]

$$\Delta \mathbf{m} = \frac{\int (\mathbf{m} - \langle \mathbf{m} \rangle_0) \exp[-\beta(U - \mathbf{M} \cdot \mathbf{F})] dX}{\int \exp[-\beta(U - \mathbf{M} \cdot \mathbf{F})] dX}, \quad (3)$$

where  $\langle \dots \rangle_{\mathbf{F}}$  and  $\langle \dots \rangle_0$  denote ensemble averages in the presence and absence of  $\mathbf{F}$ , respectively,  $\beta$  is the inverse thermal energy and  $dX$  denotes phase space integration. For small  $\mathbf{F}$ , Eq. (3) can be linearized to yield

$$\Delta \mathbf{m}(\mathbf{r}) \approx \beta [\langle \mathbf{m}(\mathbf{r}) \mathbf{M} \rangle_0 - \langle \mathbf{m}(\mathbf{r}) \rangle_0 \langle \mathbf{M} \rangle_0] \cdot \mathbf{F}. \quad (4)$$

► **Slab Geometry.** We consider a planar interfacial system with translational invariance in  $x$  and  $y$  direction, so all averaged fields and observables only depend on  $z$ .

The dielectric tensor is diagonal with only two unique components, parallel and perpendicular to the surface. Maxwell's equation  $\nabla \times \mathbf{E}(z) = 0$  implies  $\Delta E_{\parallel}(z) = E_{\parallel}$ , which shows that the tangential electric field is constant on average, i.e., neglecting field fluctuations due to, e.g., local water orientations. Eq. (1) applies to this situation, yielding the parallel dielectric response

$$\varepsilon_{\parallel}(z) = 1 + \frac{\Delta m_{\parallel}(z)}{\varepsilon_0 E_{\parallel}}. \quad (5)$$

The homogeneous field  $F_{\parallel}$  in Eq. (4) corresponds to  $E_{\parallel}$  in the parallel case. Combining Eqs. (4) and (5) gives

$$\varepsilon_{\parallel}(z) \approx 1 + \varepsilon_0^{-1} \beta [\langle m_{\parallel}(z) M_{\parallel} \rangle_0 - \langle m_{\parallel}(z) \rangle_0 \langle M_{\parallel} \rangle_0]. \quad (6)$$

For vanishing monopole density we have  $\nabla \cdot \mathbf{D}(z) = 0$  and thus the averaged perpendicular displacement field is constant,  $\Delta D_{\perp}(z) = D_{\perp}$ . To this case, Eq. (2) applies and the perpendicular dielectric response follows as

$$\varepsilon_{\perp}^{-1}(z) = 1 - \frac{\Delta m_{\perp}(z)}{D_{\perp}}. \quad (7)$$

The field  $F_{\perp}$  is associated with  $D_{\perp}/\varepsilon_0$ . Combining Eqs. (4) and (7) yields

$$\varepsilon_{\perp}^{-1}(z) \approx 1 - \varepsilon_0^{-1} \beta [\langle m_{\perp}(z) M_{\perp} \rangle_0 - \langle m_{\perp}(z) \rangle_0 \langle M_{\perp} \rangle_0]. \quad (8)$$

Whereas  $\varepsilon_{\parallel}(z)$  is irrelevant for planar systems with lateral translational invariance, it becomes crucial for the dielectric response of e.g. a point charge at an interface.

► **Simulations & Results.** We perform MD simulations (GROMACS) of pure SPC/E water in contact with two diamond surface types, one terminated with hydroxyl groups (surface coverage  $x_{\text{OH}} = 1/4$  in the notation of [19]), giving a hydrophilic surface, and one terminated with hydrogen atoms, giving a hydrophobic surface (see [19] for simulation details). Snapshots of the simulations are shown in Fig. 1, together with the number density profiles. Notably, the water density peak at the hydrophilic surface is significantly higher than at the hydrophobic surface. We calculate the dielectric response in two distinct ways: First, from polarization fluctuations without an external electric field using Eqs. (6) and (8); and second, directly from Eqs. (5) and (7) at a finite field  $\mathbf{F}$  (for which the response is a posteriori verified to be linear). To get the excess quantities  $\Delta \mathbf{E}$  and  $\Delta \mathbf{m}$ , the respective values at zero external field are subtracted.

The parallel dielectric profile  $\varepsilon_{\parallel}(z)$  is shown in Fig. 2 for a hydrophilic (a) and a hydrophobic surface (b). Solid lines depict results at vanishing external field using Eq. (6), while dashed lines follow from Eq. (5) for an external electric field of  $F_{\parallel} = E_{\parallel} = 0.05$  V/nm. The parallel polarization profile  $m_{\parallel}(z)$  is calculated directly from the boundary charge created by introducing virtual cuts in the simulation box, which is shown to be

equivalent to a summation over all multipole moments [18]. The bulk dielectric response is close to the literature value for SPC/E water of  $\varepsilon_{bulk} = 71$  [20], and the profiles from fluctuations and applied field coincide excellently. Clearly, the dielectric profiles are roughly proportional to the density profiles. This is typically assumed in coarse-grained solvation models [11], but strictly valid only for non-interacting systems. Interestingly however, the dielectric peak is higher at the hydrophobic surface compared to the hydrophilic surface, in contrast to the density, which shows the opposite trend. This disparity indicates that, although there are more polarizable molecules available in the first density peak at the hydrophilic surface, their response to an electric field is more restricted than at the hydrophobic surface. This points to a fundamental difference in dielectric response between the two surfaces, which we will get back to later. Shown as dotted lines are the dipolar dielectric contributions, calculated using only the dipole density  $\Delta\mathbf{P}_1(z)$  instead of the total polarization  $\Delta\mathbf{m}(z)$ , which agree perfectly with the full  $\varepsilon_{\parallel}(z)$  profiles, showing that quadrupole and higher order contributions are negligible for the parallel response.

The inverse perpendicular dielectric profile is shown in Fig. 2 at a hydrophilic (c) and a hydrophobic surface (d). Here we use  $E_{\perp}(z)$  to calculate  $m_{\perp}(z)$  and  $M_{\perp}$ , where  $E_{\perp}(z) = E_{\perp}(0) + \int_0^z \rho(z')/\varepsilon_0 dz'$ , with  $\rho$  the total charge density. Solid lines show the response calculated from fluctuations using Eq. (8), dashed curves represent the response to an applied electric field of  $\pm 0.5$  V/nm from Eq. (7). Again, both computational methods agree, thus confirming our formalism. Strikingly,  $\varepsilon_{\perp}^{-1}(z)$  passes through zero several times, meaning that  $\varepsilon_{\perp}(z)$  exhibits multiple singularities and extensive negative parts. This overscreening behavior is reminiscent of the non-local bulk dielectric function [2], which evidently dominates the dielectric response perpendicular to the surface, but not the parallel one. In contrast with the parallel case, the dipolar dielectric contributions (dotted lines) deviate from the full  $\varepsilon_{\perp}^{-1}(z)$  profiles, showing that here quadrupole and higher order terms are crucial. This vividly illustrates shortcomings of previous formulations [17]. Although  $\varepsilon_{\perp}^{-1}(z)$  must be related to the molecular ordering, there is no direct correlation between  $\varepsilon_{\perp}^{-1}(z)$  and the electric field stemming from the oriented molecules [18].

► **Dielectric Dividing Surface.** To interpret and apply our simulation results in a transparent fashion, we introduce the dielectric dividing surface position  $z_{\parallel}^{DDS}$ , in analogy to the Gibbs dividing surface defined by

$$z_{\parallel}^{DDS} = z_v + \int_{z_v}^{z_l} \frac{f(z_l) - f(z)}{f(z_l) - f(z_v)} dz \quad (9)$$

where  $z_v$  and  $z_l$  are positions in the vapor and liquid phase, respectively. For the Gibbs dividing surface  $z_{\parallel}^{GDS}$ ,  $f(z)$  is the fluid number density  $n(z)$ , and we obtain  $z_{\parallel}^{GDS, phob} = 0.22$  nm and  $z_{\parallel}^{GDS, phil} = 0.07$  nm, reflect-

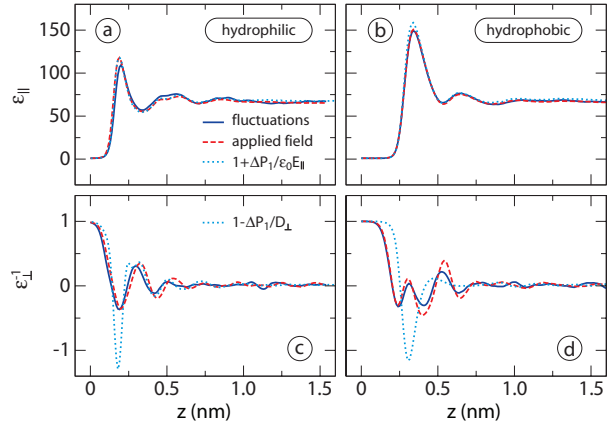


Figure 2: The parallel dielectric function  $\varepsilon_{\parallel}$  next to a hydrophilic (a) and a hydrophobic diamond (b) calculated from polarization fluctuations (Eq. (6), solid lines) and for an external electric field  $E_{\parallel} = 0.05$  V/nm (Eq. (5), dashed lines). The inverse perpendicular dielectric function  $\varepsilon_{\perp}^{-1}$  next to a hydrophilic (c) and a hydrophobic diamond (d) from fluctuations (Eq. (8), solid lines) and for an external electric field  $D_{\perp}/\varepsilon_0 = \pm 0.5$  V/nm (Eq. (7), dashed lines). The dotted lines denote the dipole contribution for an applied external field.

ing the well-known tendency for water to form a pronounced depletion layer at hydrophobic surfaces [19]. For the dielectric dividing surfaces  $z_{\parallel}^{DDS}$  and  $z_{\perp}^{DDS}$  we take  $f(z) = \varepsilon_{\parallel}(z)$ , and  $f(z) = \varepsilon_{\perp}^{-1}(z)$ , respectively, giving  $z_{\parallel}^{DDS, phil} = 0.09$  nm,  $z_{\parallel}^{DDS, phob} = 0.08$  nm,  $z_{\perp}^{DDS, phil} = 0.10$  nm and  $z_{\perp}^{DDS, phob} = 0.12$  nm. The width of the perpendicular dielectric dispersion as defined in Ref. [7] gives 0.08 nm and 0.12 nm relative to  $z = 0$  for our hydrophilic and hydrophobic profiles respectively, close to  $z_{\perp}^{DDS}$ . However, using  $z_{\perp}^{DDS}$  as the position where the permittivity changes stepwise to the bulk value, as an approximation of  $\varepsilon_{\perp}^{-1}(z)$ , always reproduces the voltage difference between  $z_l$  and  $z_v$  obtained from  $\varepsilon_{\perp}^{-1}(z)$ , which is not guaranteed when using the definition of Ref. [7]. For the dielectric shifts, defined as  $\delta_{\parallel} = z_{\parallel}^{DDS} - z_{\parallel}^{GDS}$  and  $\delta_{\perp} = z_{\perp}^{DDS} - z_{\perp}^{GDS}$ , we obtain  $\delta_{\parallel}^{phil} = 0.02 \pm 0.01$  nm and  $\delta_{\perp}^{phil} = 0.03 \pm 0.015$  nm at the hydrophilic and  $\delta_{\parallel}^{phob} = -0.14 \pm 0.01$  nm and  $\delta_{\perp}^{phob} = -0.10 \pm 0.01$  nm at the hydrophobic surface, showing a remarkable difference between the two surfaces: the dielectric interface is shifted towards the hydrophobic surface,  $\delta_{\perp}^{phob} < \delta_{\perp}^{phil}$ , indicating that water at this surface is a “better dielectric” than at the hydrophilic surface, when the reference is taken as  $z_{\parallel}^{GDS}$ . However, this difference is more than compensated by the depletion layer, which is larger at the hydrophobic surface, so that  $z_{\perp}^{DDS, phob} > z_{\perp}^{DDS, phil}$ . In the following, we compare different ways of incorporating these dielectric effects into a coarse-grained model.

► **Poisson-Boltzmann (PB) Modeling.** We consider a monovalent salt solution adjacent to a charged pla-

nar surface. Inspired by Eq. (2), we assume locality in the form  $\varepsilon_0 E_{\perp}(z) = \varepsilon_{\perp}^{-1}(z) D_{\perp}(z)$ , which is a good approximation when  $D_{\perp}(z)$  varies slowly, i.e. at low salt concentration and low surface charge density  $\sigma_0$  [6]. Taking the divergence of  $E_{\perp}(z)$  and inserting  $\nabla_z D_{\perp}(z) = P_0(z) = -2ec_0 \sinh[\beta e\psi(z)] \exp[-\mu(z)]$ , with  $\psi(z)$  the electrostatic potential and  $c_0$  the bulk salt concentration, leads to the modified PB equation,

$$\varepsilon_0 \nabla_z^2 \psi = 2ec_0 \sinh[\beta e\psi] \exp[-\mu] \varepsilon_{\perp}^{-1} - D_{\perp} \nabla_z \varepsilon_{\perp}^{-1}, \quad (10)$$

where we used  $\nabla_z \psi(z) = -E_{\perp}(z)$ . The potential  $\mu(z)$  contains all non-electrostatic surface-ion contributions such as steric and solvation effects. The displacement field follows as  $D_{\perp}(z) = \int_0^z P_0(z') dz'$ , making Eq. (10) an integro-differential equation [15, 7].

Dielectric interface effects are most crucial for the surface capacitance, defined in differential form as  $C = d\sigma_0/d\psi_0$  for  $\sigma_0 \rightarrow 0$ , where  $\psi_0 = \psi(z=0)$  is the surface potential. Fig. 3 (a) shows  $C$  calculated from Eq. (10) for different scenarios. For constant  $\varepsilon_{\perp}^{-1}(z) = \varepsilon_{bulk}^{-1}$  with  $\varepsilon_{bulk} = 71$  and  $\mu(z) = 0$  (black solid line), the calculated  $C$  grossly overestimates experimental data (black circles, for various surfaces and systems; see [18] for references), an observation that led Stern to postulate a low-dielectric surface layer [4]. Adding a generic soft ion repulsion,  $\mu(z) = \alpha \exp[1 - z/\lambda]$ , with  $\lambda$  of the order of the ionic radius,  $\lambda = 0.15$  nm, and  $\alpha = 1$ , but keeping  $\varepsilon_{\perp}^{-1}(z) = \varepsilon_{bulk}^{-1}$ , does not improve the situation much (black dotted line), irrespective of the precise values of  $\lambda$  and  $\alpha$ . On the other hand, the capacitance calculated using the full profiles  $\varepsilon_{\perp}^{-1}(z)$  (solid lines) agrees much better with experiments. Results of the sharp-kink approximation,  $\varepsilon_{\perp}^{-1}(z) = \varepsilon_{bulk}^{-1}$  for  $z > z_{\perp}^{DDS}$  and  $\varepsilon_{\perp}^{-1}(z) = 1$  otherwise (broken lines), are very close to the full profile capacitance, explaining the success of the Stern layer concept and other, more refined expressions based on the width of the dielectric dispersion (for low salt concentration) [6, 7]. Adding the soft ion repulsion  $\mu(z)$  (dotted line, only in conjunction with the sharp-kink approximation) leads to an excellent match with experiments even at high salt concentration. Note that experimentally, the capacitance increases only slightly with surface polarity [12, 18], in line with our findings at hydrophobic and hydrophilic surfaces (red and blue lines in Fig. 3 (a), respectively) and rationalized by the above-mentioned weak dominance of density depletion over interfacial dielectric effects on both surface types. The capacitance at very low salt concentration corresponds well to the value of  $3.5 \mu\text{F}/\text{cm}^2$  obtained for pure water at a platinum interface [21], despite the different water model (TIP4P and BJH) used in that study.

Note that the surface charge position at  $z = 0$  corresponds to the outermost carbon layer on the hydrophobic and to the oxygen layer on the hydrophilic surface, a crucial detail motivated by surface chemical considerations [18]. Fig. 3 (b) shows the capacitance when the charge is

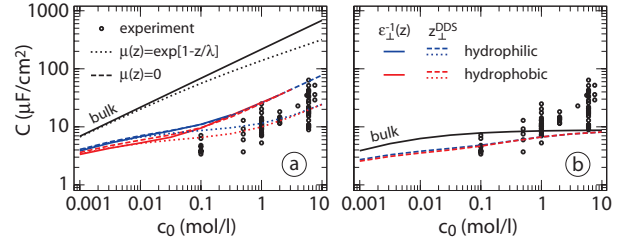


Figure 3: Double layer capacitance from Eq. (10) in the limit  $\sigma_0 \rightarrow 0$ , using  $\varepsilon_{\perp}^{-1}(z) = \varepsilon_{bulk}^{-1}$  (black lines),  $\varepsilon_{\perp}^{-1}(z)$  from MD (solid colored lines), and the sharp-kink-approximation using  $z_{\perp}^{DDS}$  (broken lines). Blue lines correspond to hydrophilic, red lines to hydrophobic surfaces. Circles denote experimental data [18]. (a) Surface charge  $\sigma_0$  located at  $z = 0$ . The dotted lines include a soft ion repulsion  $\mu(z) = \alpha \exp[1 - z/\lambda]$  and use  $\varepsilon_{bulk}^{-1}$  (black) or the sharp-kink approximation (red and blue). (b) Surface charge displaced into the substrate by  $a = 0.1$  nm with  $\varepsilon_{\perp}^{-1} = 1$  inside the substrate, using  $\varepsilon_{\perp}^{-1}(z) = \varepsilon_{bulk}^{-1}$  (solid line) and the sharp-kink approximation (dashed lines).

displaced over a distance  $a = 0.1$  nm into the substrate, using  $\varepsilon_{\perp}^{-1}(z) = 1$  for  $z < 0$ . Solid lines are calculated using  $\varepsilon_{\perp}^{-1}(z) = \varepsilon_{bulk}^{-1}$  for  $z > 0$  and dashed lines using the sharp-kink approximation. Clearly, the dependence of the capacitance on the concentration deviates from the experimental trend in both cases, supporting our initial choice of the plane of charge.

In conclusion, we establish the framework to extract the full tensorial dielectric interface profiles from MD data. The perpendicular profiles  $\varepsilon_{\perp}^{-1}(z)$  exhibit rich structure and distinct differences between hydrophobic and hydrophilic surfaces. In the context of coarse-grained PB modeling, experimental capacitance data are well reproduced. The dielectric dividing surface position is suggested as a straightforward definition of the width of a Stern layer with  $\varepsilon = 1$ . Modifications and non-linear effects are expected at higher salt concentration, which shall be addressed in the future.

## References

- [1] Israelachvili, J. & Wennerström, H. Role of hydration and water structure in biological and colloidal interactions. *Nature* **379**, 219 (1996).
- [2] Bopp, P. A., Kornyshev, A. A. & Sutmann, G. Frequency and wave-vector dependent dielectric function of water: Collective modes and relaxation spectra. *J. Chem. Phys.* **109**, 1939 (1998).
- [3] Faraudo, J. & Bresme, F. Anomalous dielectric behavior of water in ionic newton black films. *Phys. Rev. Lett.* **92**, 236102 (2004).
- [4] Stern, O. Zur Theorie der elektrolytischen Doppelschicht. *Z. Electrochem.* **30**, 508 (1924).

- [5] Tielrooij, K. J. *et al.* Dielectric relaxation dynamics of water in model membranes probed by terahertz spectroscopy. *Biophysical J.* **97**, 2484 (2009).
- [6] Kornyshev, A. A., Schmickler, W. & Vorotyntsev, M. A. Nonlocal electrostatic approach to the problem of a double layer at a metal-electrolyte interface. *Phys. Rev. B* **25**, 5244 (1982).
- [7] Kornyshev, A. A. & Vorotyntsev, M. A. Nonlocal dielectric response of the electrode/solvent interface in the double layer problem. *Can. J. Chem.* **59**, 2031 (1981).
- [8] Blum, L. & Henderson, D. Mixtures of hard ions and dipoles against a charged wall: The Ornstein-Zernike equation, some exact results, and the mean spherical approximation. *J. Chem. Phys.* **74**, 1902 (1981).
- [9] Levin, Y. Polarizable ions at interfaces. *Phys. Rev. Lett.* **102**, 147803 (2009).
- [10] Kornyshev, A. A. On the non-local electrostatic theory of hydration force. *J. Electroanal. Chem.* **204**, 79 (1986).
- [11] Dzubiella, J., Swanson, J. M. J. & McCammon, J. A. Coupling hydrophobicity, dispersion, and electrostatics in continuum solvent models. *Phys. Rev. Lett.* **96**, 087802 (2006).
- [12] Kim, Y.-T. *et al.* Drastic change of electric double layer capacitance by surface functionalization of carbon nanotubes. *Applied Phys. Lett.* **87**, 234106 (2005).
- [13] Marčelja, S. *et al.* Role of solvent structure in solution theory. *J. Chem. Soc. Faraday Trans. II* **73**, 630 (1977).
- [14] Abrashkin, A., Andelman, D. & Orland, H. Dipolar Poisson-Boltzmann equation: Ions and dipoles close to charge interfaces. *Phys. Rev. Lett.* **99**, 077801 (2007).
- [15] Paillusson, F. & Blossey, R. Slits, plates, and Poisson-Boltzmann theory in a local formulation of nonlocal electrostatics. *Phys. Rev. E* **82**, 052501 (2010).
- [16] Stillinger, F. H. & Ben-Naim, A. Liquid-vapor interface potential for water. *J. Chem. Phys.* **47**, 4431 (1967).
- [17] Ballenegger, V. & J.-P. Hansen. Dielectric permittivity profiles of confined polar fluids. *J. Chem. Phys.* **122**, 114711 (2005).
- [18] See supplementary information.
- [19] Sendner, C. *et al.* Interfacial water at hydrophobic and hydrophilic surfaces: Slip, viscosity, and diffusion. *Langmuir* **25**, 10768 (2009).
- [20] Reddy, M. R. & Berkowitz, M. The dielectric constant of SPC/E water. *Chem. Phys. Lett.* **155**, 173 (1989).
- [21] Nagy, G., Heinzinger, K. & Spohr, E. Modelling water at platinum surfaces. *Faraday Discuss.* **94**, 307 (1992).

## Supplementary Information

► **Fluctuation-Dissipation Relation.** To estimate the dielectric function from the fluctuations of the polarization, we write a statistical mechanics expression for the ensemble average excess polarization. The total interaction energy of a water-filled volume  $\mathcal{V}$  in absence of an external electric field is denoted  $U(X)$ , with  $X$  all relevant coordinates. The energy change  $\Delta U$  upon application of an external electric field  $\mathbf{F}$  is given by the coupling of the polarization to the field inside the dielectric,

$$\Delta U = \int_{\mathcal{V}} \psi(\mathbf{r}) \rho(\mathbf{r}) d\mathbf{r}, \quad (1)$$

with  $\psi$  the excess potential caused by the field,  $\nabla\psi(\mathbf{r}) = -\mathbf{F}$ , and  $\rho(\mathbf{r}) = \varepsilon_0 \nabla \cdot \mathbf{E}(\mathbf{r})$  the total charge density. The field  $\mathbf{F}$  to which the fluid responds is constant in space. Therefore, the field  $\mathbf{F}$  is associated with either  $\mathbf{E}$  or  $\mathbf{D}/\varepsilon_0$  depending on the boundary conditions. After one partial integration, the excess energy is given by

$$\Delta U = - \int_{\mathcal{V}} \nabla\psi(\mathbf{r}) \cdot \varepsilon_0 \mathbf{E}(\mathbf{r}) d\mathbf{r} = - \int_{\mathcal{V}} \mathbf{F} \cdot \mathbf{m}(\mathbf{r}) d\mathbf{r}, \quad (2)$$

where we used that  $\varepsilon_0 \mathbf{E}(\mathbf{r}) = -\mathbf{m}(\mathbf{r})$  in absence of free charges. Defining the total polarization by

$$\mathbf{M} = \int_{\mathcal{V}} \mathbf{m}(\mathbf{r}) d\mathbf{r}, \quad (3)$$

the excess polarization density upon application of the external field is given by [1, 2]

$$\begin{aligned} \Delta \mathbf{m} &= \langle \mathbf{m} \rangle_{\mathbf{F}} - \langle \mathbf{m} \rangle_0 \\ &= \frac{\int (\mathbf{m} - \langle \mathbf{m} \rangle_0) \exp[-\beta(U - \mathbf{M} \cdot \mathbf{F})] dX}{\int \exp[-\beta(U - \mathbf{M} \cdot \mathbf{F})] dX}, \end{aligned} \quad (4)$$

where  $\langle \dots \rangle_{\mathbf{F}}$  and  $\langle \dots \rangle_0$  denote ensemble averages with and without applied electric field, respectively. For molecules without atomic polarizability, the phase space integration in Eq. 4 involves the positions and orientations of the permanent multipole moments,  $dX = \prod_i d\mathbf{r}_i d\Omega_i$ , with  $i$  the molecular index. For small field  $\mathbf{F}$ , Eq. 4 can be linearized to yield

$$\Delta \mathbf{m} \approx \frac{\int (\mathbf{m} - \langle \mathbf{m} \rangle_0) (1 + \beta \mathbf{M} \cdot \mathbf{F}) \exp[-\beta U] dX}{\int \exp[-\beta U] dX}, \quad (5)$$

or, using the short notation for the ensemble average,

$$\Delta \mathbf{m}(\mathbf{r}) \approx \beta [\langle \mathbf{m}(\mathbf{r}) \mathbf{M} \rangle_0 - \langle \mathbf{m}(\mathbf{r}) \rangle_0 \langle \mathbf{M} \rangle_0] \cdot \mathbf{F}. \quad (6)$$

Eq. 6 gives all nine components of the excess polarization separately.

► **Calculation of the Parallel Displacement Field.** Gauss's integral equation for the displacement field reads

$$\oint_{\partial \mathcal{V}} \mathbf{D}(\mathbf{r}) \cdot \hat{\mathbf{n}}(\mathbf{r}) d\mathbf{r} = \int_{\mathcal{V}} P_0(\mathbf{r}) d\mathbf{r}, \quad (7)$$

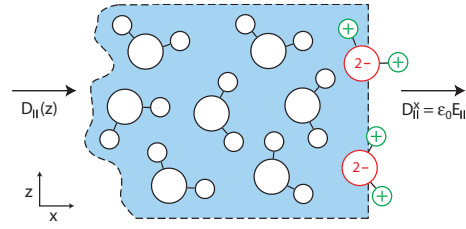


Figure S1: Schematic picture of the Gauss volume used for the integration of Eq. 7. On the left-hand side, the volume has been chosen such that water molecules are not split across the boundary, whereas on the right-hand side the water box is cut perpendicular to the  $x$ -axis.

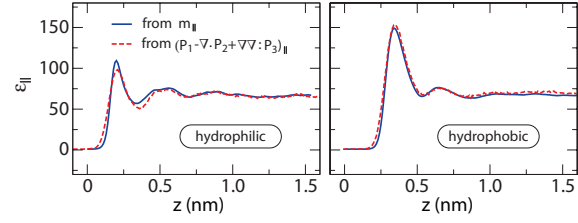


Figure S2: The dielectric response calculated from the polarization  $m_{\parallel}(z)$  using Eq. 10 (solid lines), and from an explicit evaluation of the multipole moments up to the octupole term using Eq. 4 in the main text (dashed lines). The response is calculated using the fluctuation equation (Eq. 8 in the main text). The left panel corresponds to the hydrophilic surface and the right panel to the hydrophobic surface.

which holds for any volume  $\mathcal{V}$ . To calculate the displacement field in  $x$ -direction we cut the simulation box perpendicular to the  $x$ -axis. Because we cut some water molecules, we create a non-zero monopole density on both sides of the cut. Now we perform the integration of Eq. 7 over a volume as depicted in Fig. S1, where the water molecules have been cut on one side, but not on the other. On the left-hand side of this volume, the displacement field is still  $D_{\parallel}(z)$  because of translational invariance, whereas at the position of the cut it has been changed by the creation of the monopole density. Integrating Eq. 7 gives

$$\left[ D_{\parallel}^x(z) - D_{\parallel}(z) \right] \mathcal{S} = \int_{\mathcal{V}} P_0(z) d\mathbf{r}, \quad (8)$$

with  $D_{\parallel}^x(z)$  the displacement field at the position of the cut and  $\mathcal{S}$  the surface area of the cut. Taking the divergence of Eq. 8 shows that  $D_{\parallel}^x$  is independent of  $z$ , because  $\nabla_z D_{\parallel}(z) = P_0(z)$  and  $\nabla_z \int_{\mathcal{V}} P_0(z) d\mathbf{r} = P_0(z) \mathcal{S}$ . In vacuum,  $P_0(z)$  vanishes and  $D_{\parallel}(z) = \varepsilon_0 E_{\parallel}$ . Therefore,

$$D_{\parallel}(z) = \varepsilon_0 E_{\parallel} - \frac{1}{\mathcal{S}} \int_{\mathcal{V}} P_0(z) d\mathbf{r}, \quad (9)$$

and thus

$$m_{\parallel}(z) = -\frac{1}{\mathcal{S}} \int_{\mathcal{V}} P_0(z) d\mathbf{r}. \quad (10)$$

Eq. 10 can be verified using an alternative reasoning. The polarization  $\mathbf{m}(\mathbf{r})$  can be written as

$$\begin{aligned}\mathbf{m}(\mathbf{r}) &= -\frac{1}{4\pi} \int \mathbf{m}(\mathbf{r}') \cdot \nabla' \frac{\mathbf{r} - \mathbf{r}'}{|\mathbf{r} - \mathbf{r}'|^3} d\mathbf{r}' \\ &= -\frac{1}{4\pi} \nabla \int \mathbf{m}(\mathbf{r}') \cdot \nabla' \frac{1}{|\mathbf{r} - \mathbf{r}'|} d\mathbf{r}'.\end{aligned}\quad (11)$$

Partial integration gives

$$\begin{aligned}\mathbf{m}(\mathbf{r}) &= -\frac{1}{4\pi} \nabla \left[ \int \nabla' \cdot \frac{\mathbf{m}(\mathbf{r}')}{|\mathbf{r} - \mathbf{r}'|} d\mathbf{r}' \right. \\ &\quad \left. - \int \frac{\nabla' \cdot \mathbf{m}(\mathbf{r}')}{|\mathbf{r} - \mathbf{r}'|} d\mathbf{r}' \right].\end{aligned}\quad (12)$$

Transforming the first integral of Eq. 12 leads to

$$\begin{aligned}\mathbf{m}(\mathbf{r}) &= -\frac{1}{4\pi} \nabla \left[ \oint \frac{\mathbf{m}(\mathbf{r}') \cdot \hat{\mathbf{n}}}{|\mathbf{r} - \mathbf{r}'|} d\mathbf{r}' \right. \\ &\quad \left. - \int \frac{\nabla' \cdot \mathbf{m}(\mathbf{r}')}{|\mathbf{r} - \mathbf{r}'|} d\mathbf{r}' \right],\end{aligned}\quad (13)$$

which has two parts: the first scales like the field from a surface charge density  $\sigma(\mathbf{r}) = -\mathbf{m}(\mathbf{r}) \cdot \hat{\mathbf{n}}$ , and the second like the field from a volume charge density  $\rho(\mathbf{r}) = \nabla \cdot \mathbf{m}(\mathbf{r})$ . When cutting the volume (for example in the way indicated in Fig. S1, but it can be cut in any way), the only charge density scaling like a surface charge density is the charge density created by cutting the water molecules. Therefore, the surface charge density  $\sigma(\mathbf{r})$  must be equal to

$$\sigma(\mathbf{r}) = \frac{1}{S} \int_{\mathcal{V}} P_0(\mathbf{r}) d\mathbf{r}, \quad (14)$$

confirming Eqs. 9 and 10.

As evidence of the equivalence of the polarization as calculated from Eq. 10, and the polarization calculated from summing all multipole fields explicitly (Eq. 4 in the main text), we show the dielectric response calculated with both methods in Fig. S2. The dielectric response is calculated using the fluctuation equation (Eq. 8 in the main text). The curves coincide, thus confirming the validity of our method.

### ► On the Molecular Origin of the Structure of the Perpendicular Response.

Clearly, the structure of the perpendicular dielectric response function  $\varepsilon_{\perp}^{-1}(z)$  is related to the collective ordering and orientation of the polar molecules at the interface. To see whether there may be a simple relation between the perpendicular response  $\varepsilon_{\perp}^{-1}(z)$  and the electric field caused by the ordering and orientation of the water molecules in absence of an external field  $E_{\perp}$ , we plot both functions in Fig. S3. There is no direct correlation between the two quantities, showing that the shape of the response function is non-trivial and not related to the equilibrium polarization of interfacial water in any simple or obvious way.

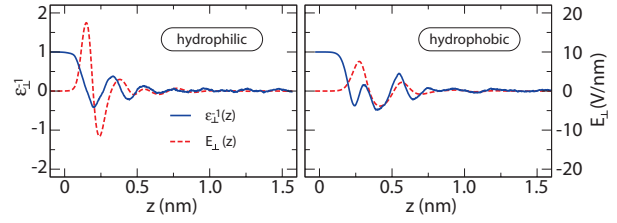


Figure S3: The perpendicular dielectric response  $\varepsilon_{\perp}^{-1}(z)$  as a function of  $z$  (solid lines) at a hydrophilic (left) and a hydrophobic surface (right). Also shown is the electric field  $E_{\perp}(z)$  caused by the oriented water molecules at the interface in absence of an external field (dashed lines), showing no direct correlation with the dielectric response.

► **Pressure Between Parallel Plates.** The electrostatic potential  $\psi(z)$  between two plates is calculated from the modified Poisson-Boltzmann equation,

$$\varepsilon_0 \nabla_z^2 \psi = 2ec_0 \sinh[\beta e\psi] \exp[-\mu] \varepsilon_{\perp}^{-1} - D_{\perp} \nabla_z \varepsilon_{\perp}^{-1}, \quad (15)$$

with  $c_0$  the bulk salt concentration,  $\mu(z)$  a non-electrostatic ion-wall potential,  $\beta$  the inverse thermal energy and  $e$  the absolute charge of an electron. The displacement field is calculated as the integral over the monopole density  $P_0(z) = -2ec_0 \sinh[\beta e\psi(z)] \exp[-\mu(z)]$ ,

$$D_{\perp}(z) = \int_0^z P_0(z') dz'. \quad (16)$$

For the dielectric profile between the two plates we join the  $\varepsilon_{\perp}^{-1}(z)$  profiles from both surfaces piecewise. We calculate the disjoining pressure between two plates from the free energy [3, 4, 5, 6],

$$\beta\mathcal{F} = \int \frac{\beta\psi}{2} P_0 + \sum_{\pm} c_{\pm} \left[ \mu + \log \frac{c_{\pm}}{c_0} - 1 \right] dz + \beta\sigma_0\psi_0, \quad (17)$$

with  $\sigma_0$  the surface charge density,  $\psi_0$  the potential at the wall and  $c_{\pm} = c_0 \exp[\mp\beta e\psi - \mu]$  the ionic density. The pressure between two plates at separation  $d$  is given by

$$\beta p(d) = -\frac{d\beta\mathcal{F}}{dd} - 2c_0. \quad (18)$$

### ► Experimental Values of the Double Layer Capacitance.

This section contains an overview of published experimental values of the double layer capacitance on various carbon-based surfaces in aqueous electrolytes. The capacitance of the electrical double layer is measured using cyclic voltammetry or AC impedance spectroscopy. The accessible surface area is determined using  $N_2$  adsorption.

In the tables below, we grouped the different measurements based on the contact angle in aqueous solution. When below  $90^\circ$ , the substrate is classified as hydrophilic (listed in Tab. S1), otherwise as hydrophobic (listed in Tab. S2). Materials of which the contact angle

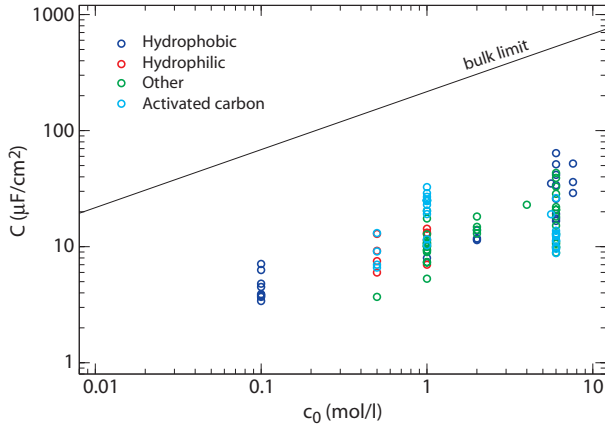


Figure S4: Double layer capacitance as a function of bulk concentration, showing all data points from Tabs. S2, S1, S3 and S4, as well as the bulk value of the capacitance, calculated using  $\varepsilon_{bulk} = 71$  and  $\mu(z) = 0$ .

is unknown or unclear are displayed in Tab. S3. All data are plotted as a function of electrolyte concentration in Fig. S4. The scattering in the data between substrates and electrolytes is larger than the structural difference between hydrophilic and hydrophobic substrates. Nevertheless, when a specific substrate is modified to become more hydrophilic, for example using functional groups or doping, the double layer capacitance increases [7, 8]. In addition, we show the limiting “bulk” value of the differential double layer capacitance  $C = d\sigma_0/d\psi_0$ , calculated from Eq. 15 using the bulk dielectric constant  $\varepsilon_{\perp}^{-1}(z) = \varepsilon_{bulk}^{-1}$  with  $\varepsilon_{bulk} = 71$  for the entire fluid and  $\mu(z) = 0$ . For all substrates, the capacitance is much lower than the bulk value.

Many of the materials used for double layer capacitors belong to the class of so-called activated carbons, which are treated with a gas plasma or a strong acid or base solution to make the surface more porous. While increasing the total capacitance of the sample, activation of a carbon surface often decreases the capacitance per unit surface area dramatically [9, 10]. Although the mechanism leading to this decrease is unclear, we can safely assume that a part of the additional surface area created by the activation process is inaccessible to the electrolyte, and therefore does not contribute to the double layer capacitance. Because of these poorly defined surface characteristics, we do not include the activated carbons in Fig. 3 (a) of the main paper. Therefore, Fig. 3 (a) only contains the data from Tabs. S2, S1 and S3.

► **On the Plane of Charge.** The exact location of the surface charge density on the substrate has an influence on the total measured capacitance. For Fig. 3 of the main paper, the charge density is placed at the position of the outermost heavy solid atom, which is the oxygen in case of the hydrophilic surface and the outermost carbon atom in case of the hydrophobic surface. Provided that charges inside the solid are mobile, these positions

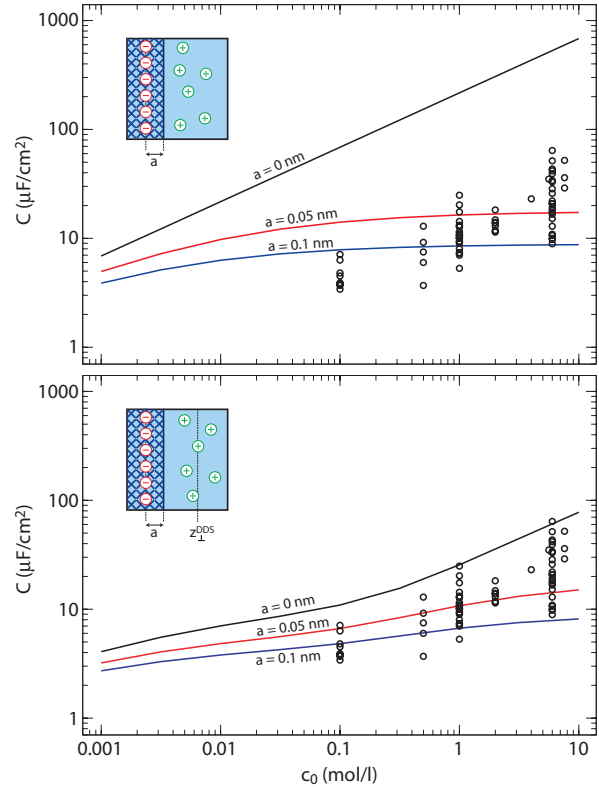


Figure S5: Total capacitance of the double layer for different positions  $a$  of the charge inside the substrate as a function of the bulk salt concentration  $c_0$ . Top: the dielectric function is equal to the bulk value everywhere,  $\varepsilon_{\perp}^{-1}(z) = \varepsilon_{bulk}^{-1}$  with  $\varepsilon_{bulk} = 71$  everywhere in the fluid and 1 inside the substrate. Bottom: the dielectric function is  $\varepsilon_{\perp}^{-1}(z) = \varepsilon_{bulk}^{-1}$  for  $z > z_{\perp}^{DDS} = 0.1$  nm and 1 elsewhere. In the insets, we show a schematic image of the substrate with the plane of charge located at a distance  $a$  from the aqueous interface.

make most sense chemically. In addition, this is the position where the charge density would be placed in an atomistic simulation. Fig. S5 shows the dependence of the capacitance on the distance  $a$  between the plane of charge and the position of the outermost solid atom. No additional repulsive potential is used and the dielectric constant of the substrate is set equal to 1. Obviously, changing  $a$  and the dielectric constant of the substrate simultaneously would lead to similar results. In the top panel, the dielectric constant is kept equal to the bulk value everywhere,  $\varepsilon_{\perp}^{-1}(z) = \varepsilon_{bulk}^{-1}$  with  $\varepsilon_{bulk} = 71$ . When the charge is moved further inside the substrate (increasing  $a$ ), the capacitance goes down, but at the same time, the dependence of the capacitance on the salt concentration changes dramatically. Clearly, the concentration dependence of the experimental data (black circles) can not be reproduced by only assuming a finite displacement of the charge inside the substrate. In the bottom panel, we show the same curves, now using the sharp-kink approximation of the dielectric profile:  $\varepsilon_{\perp}^{-1}(z) = \varepsilon_{bulk}^{-1}$  for  $z > z_{\perp}^{DDS} = 0.1$  nm and  $\varepsilon_{\perp}^{-1} = 1$  otherwise. The curve for

$a = 0$  is already shown in Fig. 3 (a) of the main paper. Although the capacitance for small  $a$  still reproduces the experimental data, the concentration dependence of the curves deviates from the experimental trend.

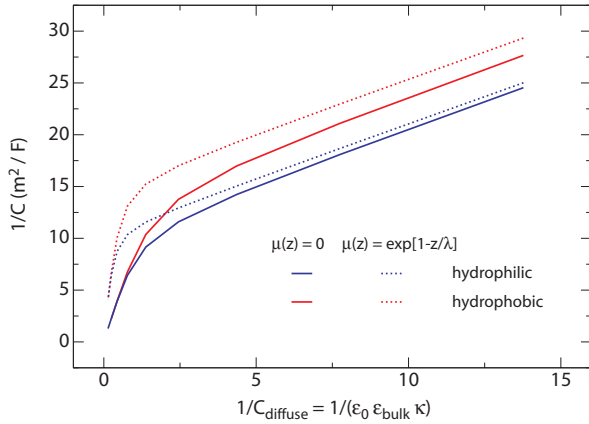


Figure S6: The inverse capacitance  $C^{-1}$ , calculated from Eq. 15, of a system with  $\varepsilon_{\perp}^{-1}(z) = 1$  until  $z = z_{\perp}^{\text{DDS}}$  and  $\varepsilon_{\perp}^{-1}(z) = \varepsilon_{\text{bulk}}^{-1}$  with  $\varepsilon_{\text{bulk}} = 71$  afterwards for hydrophilic ( $z_{\perp}^{\text{DDS}} = 0.1$  nm) and hydrophobic ( $z_{\perp}^{\text{DDS}} = 0.12$  nm) surfaces, plotted as a function of the inverse diffuse layer capacitance from Eq. 19. We used  $\mu(z) = 0$  (solid lines), as well as a mild repulsive potential  $\mu(z) = \alpha \exp[1 - z/\lambda]$  with  $\alpha = 1$  and  $\lambda = 0.15$  nm (dotted lines).

► **Parsons-Zobel Plot.** The capacitance according to the Gouy-Chapman model of a solid-electrolyte interface at low surface potential is easily calculated from the Debye-Hückel equation as

$$C_{\text{diffuse}} = \varepsilon_0 \varepsilon_{\text{bulk}} \kappa, \quad (19)$$

with the inverse Debye screening length given by

$$\kappa = \sqrt{\frac{2e^2 c_0}{\varepsilon_0 \varepsilon_{\text{bulk}} k_B T}}. \quad (20)$$

Plotting the measured inverse capacitance as a function of the inverse of the expression in Eq. 19 gives a clear visualization of the deviation of the Gouy-Chapman theory from experimental data [11, 12]. Experimentally, the curve is found to be linear, with slope 1, for high values of  $C_{\text{diffuse}}^{-1}$  (low salt concentration  $c_0$ ), dropping towards zero for higher salt concentrations [13]. The interception point of the linear extrapolation of the curve at low salt concentration with the line  $C_{\text{diffuse}}^{-1} = 0$  can be interpreted as the inverse of the Stern layer capacitance which is placed in series with the diffuse layer capacitance. In Fig. S6, we present a Parsons-Zobel plot of our theoretical curves of the capacitance for the Stern layer model:  $\varepsilon_{\perp}^{-1}(z) = 1$  until  $z = z_{\perp}^{\text{DDS}}$  and  $\varepsilon_{\perp}^{-1}(z) = \varepsilon_{\text{bulk}}^{-1}$  afterwards. Qualitatively, the curves agree with the experimental results.

## References

- [1] Fröhlich, H. *Theory of Dielectrics* (Clarendon Press, Oxford, 1949).
- [2] Ballenegger, V. & J.-P. Hansen. Dielectric permittivity profiles of confined polar fluids. *J. Chem. Phys.* **122**, 114711 (2005).
- [3] Lyklema, J. *Fundamentals of Interface and Colloid Science, Vol I* (Academic Press, London, 1991).
- [4] Lyklema, J. *Fundamentals of Interface and Colloid Science, Vol II* (Academic Press, London, 1995).
- [5] Andelman, D. Introduction to electrostatics in soft and biological matter. In Poon, W. & Andelman, D. (eds.) *Soft Condensed Matter Physics in Molecular and Cell Biology*, 97. Nato ASI & SUSSP (Taylor & Francis, New York, 2006).
- [6] Edwards, S. A. & Williams, D. R. M. Double layers and interparticle forces in colloid science and biology: Analytic results for the effect of ionic dispersion forces. *Phys. Rev. Lett.* **92**, 248303 (2004).
- [7] Kim, Y.-T. *et al.* Drastic change of electric double layer capacitance by surface functionalization of carbon nanotubes. *Applied Phys. Lett.* **87**, 234106 (2005).
- [8] Kwon, T. *et al.* Enhancement mechanism of electrochemical capacitance in nitrogen-/boron-doped carbons with uniform straight nanochannels. *Langmuir* **25**, 11961 (2009).
- [9] Jiang, J. *et al.* Enhanced electrical capacitance of porous carbons by nitrogen enrichment and control of the pore structure. *Microporous Mesoporous Mater.* **118**, 28 (2009).
- [10] Wang, H., Gao, Q. & Hu, J. Preparation of porous doped carbons and the high performance in electrochemical capacitors. *Microporous Mesoporous Mater.* **131**, 89 (2010).
- [11] Kornyshev, A. A. & Ulstrup, J. Solvent structural effect on the deviation from linear Parsons-Zobel plots with increasing electrolyte concentration. *J. Electroanal. Chem.* **183**, 387 (1985).
- [12] Blum, L., Henserson, D. & Parsons, R. The mean spherical approximation capacitance of the double layer for an electrolyte at high concentration. *J. Electroanal. Chem.* **161**, 389 (1984).
- [13] Parsons, R. & Zobel, F. G. R. The interphase between mercury and aqueous sodium dihydrogen phosphate. *J. Electroanal. Chem.* **9**, 333 (1965).
- [14] Artemenko, S. E., Glukhova, L. G. & Zagoruiko, N. I. Effect of oxidative treatment of carbon fibre on the properties of a carbon-fibre-filled plastic fab-

- ricated by polycondensation filling. *Fibre Chemistry* **33**, 502 (2001).
- [15] Okajima, K., Ohta, K. & Sudoh, M. Capacitance behavior of activated carbon fibers with oxygen-plasma treatment. *Electrochim. Acta* **50**, 2227 (2005).
- [16] Frackowiak, E. *et al.* Optimisation of supercapacitors using carbons with controlled nanotexture and nitrogen content. *Electrochim. Acta* **51**, 2209 (2006).
- [17] Sidorenko, A. *et al.* Switching of polymer brushes. *Langmuir* **15**, 8349 (1999).
- [18] Harnish, B. *et al.* UV-cross-linked poly(vinylpyridine) thin films as reversibly responsive surfaces. *Chem. Mater.* **17**, 4092 (2005).
- [19] Goeting, C. H. *et al.* Sonoelectrochemistry at tungsten-supported boron-doped CVD diamond electrodes. *Diamond Relat. Mater.* **8**, 824 (1999).
- [20] Swain, G. M. & Ramesham, R. The electrochemical activity of boron-doped polycrystalline diamond thin film electrodes. *Anal. Chem.* **65**, 345 (1993).
- [21] Kocrick, E. *et al.* Ordered mesoporous carbide derived carbons for high pressure gas storage. *Carbon* **48**, 1707 (2010).
- [22] Fernández, J. A. *et al.* EDLC performance of carbide-derived carbons in aprotic and acidic electrolytes. *Electrochim. Acta* **53**, 7111 (2008).
- [23] Wang, S. *et al.* Wettability and surface free energy of graphene films. *Langmuir* **25**, 11078 (2009).
- [24] Li, H.-Q. *et al.* A competitive candidate material for aqueous supercapacitors: High surface-area graphite. *J. Power Sources* **185**, 1557 (2008).
- [25] Du, X. *et al.* Graphene nanosheets as electrode material for electric double-layer capacitors. *Electrochim. Acta* **55**, 4812 (2010).
- [26] Pandolfo, A. G. & Hollenkamp, A. F. Carbon properties and their role in super-capacitors. *J. Power Sources* **157**, 11 (2006).
- [27] Chen, W.-C. & Wen, T.-C. Electrochemical and capacitive properties of polyaniline-implanted porous carbon electrode for supercapacitors. *J. Power Sources* **117**, 273 (2003).
- [28] Karandikar, P. *et al.* Synthesis and characterization of mesoporous carbon through inexpensive mesoporous silica as template. *Microporous Mesoporous Mater.* **98**, 189 (2007).
- [29] Sevilla, M. *et al.* Performance of templated mesoporous carbons in supercapacitors. *Electrochim. Acta* **52**, 3207 (2007).
- [30] Fuertes, A. B., Pica, F. & Rojo, J. M. Influence of pore structure on electric double-layer capacitance of template mesoporous carbons. *J. Power Sources* **133**, 329 (2004).
- [31] Fuertes, A. B. *et al.* Templated mesoporous carbons for supercapacitor application. *Electrochim. Acta* **50**, 2799 (2005).
- [32] Cao, Y. *et al.* Synthesis, characterization, and electrochemical properties of ordered mesoporous carbons containing nickel oxide nanoparticles using sucrose and nickel acetate in a silica template. *J. Solid State Chem.* **180**, 792 (2007).
- [33] Kalpana, D. *et al.* Recycled waste paper – a new source of raw material for electric double-layer capacitors. *J. Power Sources* **190**, 587 (2009).
- [34] Zhou, H. *et al.* Electrochemical capacitance of self-ordered mesoporous carbon. *J. Power Sources* **122**, 219 (2003).
- [35] Xu, B. *et al.* High-capacitance carbon electrode prepared by PVDC carbonization for aqueous EDLCs. *Electrochim. Acta* **54**, 2185 (2009).
- [36] Ramesham, R. & Rose, M. F. Electrochemical characterization of doped and un-doped CVD diamond deposited by microwave plasma. *Diamond Relat. Mater.* **6**, 17 (1997).
- [37] Roldán, S. *et al.* Comparison between electrochemical capacitors based on NaOH- and KOH-activated carbons. *Energy Fuels* **24**, 3422 (2010).
- [38] Seredych, M. *et al.* Surface functional groups of carbons and the effects of their chemical character, density and accessibility to ions on electrochemical performance. *Carbon* **46**, 1475 (2008).

Table S1: Double layer capacitance of hydrophilic carbon-based materials.

Surface material	Contact angle ( $^{\circ}$ )	Electrolyte	Concentration (M)	Capacitance ( $\mu\text{F}/\text{cm}^2$ )	Ref.
Carbon fibers	24 - 37 [14]	$\text{H}_2\text{SO}_4$	0.5	6.0	[15] <sup>a</sup>
				7.5	
				9.2	
				12.9	
Carbon-coated $\text{Al}_2\text{O}_3$	57	$\text{H}_2\text{SO}_4$	1	7.0	[8]
Nitrogen-doped	41			11.4	
Boron-doped	60			12.9	
Oxidated polyvinylpyridine	45 - 67	$\text{H}_2\text{SO}_4$	1	13.2	[16]
Blend with coal tar pitch	[17, 18]			14.3	

<sup>a</sup>Different values correspond to different commercial samples (untreated).

Table S2: Double layer capacitance of hydrophobic carbon-based materials.

Surface material	Contact angle ( $^{\circ}$ )	Electrolyte	Concentration (M)	Capacitance ( $\mu\text{F}/\text{cm}^2$ )	Ref.
Boron-doped diamond	> 90 [19]	$\text{H}_2\text{SO}_4$	0.1	3.7	[20] <sup>a</sup>
				7.1	
		KCl	0.1	3.4	
				4.5	
		$\text{NaNO}_3$	0.1	3.8	
				6.3	
NaOH	0.1	3.9			
		4.8			
Carbide-derived carbon TiC, TiC & SiC/TiC	> 90 [21]	$\text{H}_2\text{SO}_4$	2	11.4	[22]
				13.8	
				11.8	
Graphite	98 [23]	KOH	6	17.5	[24] <sup>b</sup>
				16.7	
				19.2	
				25.9	
				33.9	
				41.6	
				51.4	
64.0					
Graphene nanosheets	127 [23]	KOH	7.6	29	[25]
				26	
				52	
Carbon black		$\text{H}_2\text{SO}_4$	1	8	[26]
Graphite powder		NaCl	5.6	35	

<sup>a</sup>The different values correspond to AC impedance and cyclic voltametry measurements, respectively.

<sup>b</sup>The surface area of natural graphite was increased using ball-milling; different values correspond to different milling times.

Table S3: Double layer capacitance of materials with unknown contact angle.

Surface material	Electrolyte	Concentration (M)	Capacitance ( $\mu\text{F}/\text{cm}^2$ )	Ref.
Porous carbon	$\text{H}_2\text{SO}_4$	1	5.3	[27]
Porous carbon with polyaniline			9.0	
Silica-templated mesoporous carbon	$\text{H}_2\text{SO}_4$	1	12.8	[16]
			10.1	
			7.4	
			9.3	
			11.4	
			9.4	
Silica-templated mesoporous carbon	$\text{H}_2\text{SO}_4$	1	7.3	[28]
		2	14	[29]
		2	13	[30]
Silica-templated mesoporous carbon	$\text{H}_2\text{SO}_4$	1	10.2	[31]
			10.6	
			10.7	
			10.9	
	KOH	6	9.8	
			10.9	
			8.9	
			10.6	
Mesoporous carbon with NiO	KOH	2	18.2	[32]
Carbon aerogel	KOH	4	23	[26]
	KOH	6	28.5	[33]
Porous carbon	KOH	6	33	[10]
Self-ordered mesoporous carbon	$\text{LiPF}_6$	1	10	[34]
Nitrogen-containing mesoporous carbon	KOH	6	39.2	[9]
Ordered mesoporous carbon			10.0	
Porous carbon from carbonization of poly(vinylidene chloride)	KOH	6	20.8	[35]
			22.0	
			20.8	
			18.2	
			15.2	
			12.9	
Diamond film	NaCl	0.5	3.7	[36] <sup>a</sup>
Polyacrylonitrile	$\text{H}_2\text{SO}_4$	1	24.9	[16]
Blend with coal tar pitch			20.3	
			17.5	
TiC/TiO <sub>2</sub>	$\text{H}_2\text{SO}_4$	2	14.8	[22]
Carbon composite from waste paper	KOH	6	43.2	[33]

<sup>a</sup>After equilibration in electrolyte, assuming complete wetting at the maximum of the capacitance.

Table S4: Double layer capacitance of different kinds of activated carbons.

Surface material	Electrolyte	Concentration (M)	Capacitance ( $\mu\text{F}/\text{cm}^2$ )	Ref.
CO <sub>2</sub> activated porous carbon	KOH	6	13	[10]
			9.6	
KOH activated porous carbon			10	
			8.8	
Nitrogen-containing mesoporous carbon, activated with KOH	KOH	6	26.2	[9]
			13.7	
			11.3	
Ordered mesoporous carbon, activated with KOH	KOH	6	11.2	[9]
			12.7	
			12.4	
KOH-activated carbon	H <sub>2</sub> SO <sub>4</sub>	1	20.4	[37]
			25.1	
			26.9	
NaOH-activated carbon			24.7	
			25.0	
			28.9	
Wood origin HNO <sub>3</sub> -activated carbon	H <sub>2</sub> SO <sub>4</sub>	1	11.6	[38]
			10.3	
			19.1	
			25.5	
			23.0	
			32.6	
Activated carbon	NaCl	5.6	19	[26]
O <sub>2</sub> -activated carbon fibers			6.6	[15]
			7.0	
			9.1	
			13.2	